Cell Biochem Biophys
DOI 10.1007/s12013-016-0760-7

ORIGINAL PAPER

A Simple Analytical Approximation to an Inhomogeneously-Broadened Dispersion Spectrum. Application to Absorption-Dispersion Admixtures

Barney L. Bales[1]

Received: 21 August 2016 / Accepted: 24 August 2016

Abstract A simple analytical approximation to an inhomogeneously-broadened dispersion signal is proposed and tested with resonance lines broadened by unresolved hyperfine structure. Spectral parameters may be rapidly and accurately extracted using a nonlinear least-squares fitting algorithm. Combining the new approximation to a dispersion signal with a well-known approximation to the absorption signal allows dispersion-absorption admixtures, a problem of growing importance, to be analyzed quickly and accurately. For pure dispersion signals, the maximum difference between the fit and the signal for unresolved lines is 1.1 % of the maximum intensity. For pure absorption, the difference is 0.33 % of the peak-to-peak intensity, and for admixtures up to 40 % dispersion (maximum intensity/peak-to-peak intensity), the difference is 0.7 %. The accuracy of the recovered spectral parameters depends on the degree of inhomogeneously-broadened and the percentage admixture, but they are generally about 1 % at most. A significant finding of the work is that the parameters pertinent to the dispersion or the absorption are insignificantly different when fitting isolated lines vs. fitting admixtures. Admixtures with added noise or an unsuspected extraneous line are investigated.

Keywords EPR · Nitroxide spin labels · Inhomogeneously-broadened dispersion spectra · Absorption-dispersion admixtures

✉ Barney L. Bales
barney.bales@csun.edu

[1] Department of Physics and Astronomy, California State University at Northridge, Northridge, CA 91330, USA

Introduction

The Voigt line shape, a convolution of Lorentzian and Gaussian shapes, has been used to model unresolved electron paramagnetic resonance (EPR) absorption lines for more than 85 years, [1] as well as absorption lines in other fields [2–5] The Lorentzian component contains information about the spin relaxation, the Gaussian being due to inhomogeneous broadening (IHB), often caused by unresolved hyperfine structure [6] or magnetic-field modulation [7]. See Table 1 for a list of definitions, abbreviations and acronyms. The first-derivative of the cw-EPR spectrum is normally presented and will be assumed in this paper. Explicit expressions for the Voigt[1] absorption are given by Eqs. (5) or (6) of ref [6]. The shape is uniquely determined by the Voigt parameter [6]

$$\chi \equiv \frac{\Delta H_{pp}^{G}}{\Delta H_{pp}^{L}} \tag{1}$$

where ΔH_{pp}^{G} and ΔH_{pp}^{L} are the peak-to-peak line widths of the Gaussian and Lorentzian components, respectively [6]. The IHB is quantified by ΔH_{pp}^{G}; thus, as IHB increases, so does χ.

Detailed procedures to correct parameters extracted from absorption IHB nitroxide free-radical (nitroxide) spectra as a function of χ were given in a review, [6] which relied on measurements of four points on the spectrum. Later [8],

[1] To simplify the presentation, we abbreviate the Voigt, Lorentzian, Gaussian, and sum-function line shape functions as simply the Voigt, Lorentzian, Gaussian, and sum-function, respectively. To distinguish between the absorption and dispersion, we refer, to the Voigt absorption or the Lorentzian dispersion, etc. Furthermore, we shall write that "ΔH_{pp}^{0} increases …" rather than "the value of ΔH_{pp}^{0} increases …," etc.

Published online: 19 September 2016

Table 1 Definitions, abbreviations, and acronyms

Absorption manifold, dispersion manifold	A hyperfine pattern with a first-derivative Lorentzian absorption or dispersion imposed upon each line, respectively.
Pattern	Hyperfine pattern
ΔH_{pp}^{G}, ΔH_{pp}^{L}	Known input values of the peak-to-peak line widths of the Gaussian and Lorentzian components of a manifold, respectively
ΔH_{pp}^{0}	Predicted peak-to-peak line width of a manifold computed from known input values of ΔH_{pp}^{G} and ΔH_{pp}^{L}, Eq. (9a).
ΔH_{pp}^{fit}	ΔH_{pp}^{0} as fit by Eqs (2), (11), (16), or (20), respectively
$\Delta H_{pp}^{G}(fit)$, $\Delta H_{pp}^{L}(fit)$	Gaussian, Lorentzian line widths derived from ΔH_{pp}^{fit} and the map in Fig. 8.
V_{disp}	Known input value of sum of the maximum intensities of the Lorentzian dispersions of a dispersion manifold
V_{pp}	Known input value of the sum of the peak-to-peak intensities of the Lorentzian absorptions of an absorption manifold
V_{man}^{disp}, V_{pp}^{man}	Directly measured values of the maximum intensity of the dispersion and the peak-to-peak intensity of the absorption manifolds, respectively
V_{disp}^{fit}, V_{pp}^{fit}	Approximations to V_{disp}^{man} or V_{pp}^{man} of manifolds as fit by Eqs (2), (11), (16), or (20), respectively
$Y_{disp}^{sum'}$, $Y_{abs}^{sum'}$, $Y_{mix}^{sum'}$	Sum-function approximations to dispersion, absorption, and admixture manifolds, respectively
Voigt(s), Lorentzian(s), Gaussian(s), Sum-function(s)	First-derivative Voigt, Lorentzian, Gaussian, or sum-function line shape function(s), respectively. These are used as adjectives to modify dispersion or absorption. For example, we refer to Voigt dispersion(s) or Lorentzian absorption(s), etc.
Fit	Verb, performing a least-squares fit; Noun, the result of the fit
IHB	Inhomogeneously broadened
Nitroxide(s)	Nitroxide free radical(s)

these procedures were extended to non-linear least-squares fits of the entire spectrum.

The four-point method is significantly better than ignoring the IHB as detailed in ref [6], but is of poor accuracy for noisy spectra and is not directly applicable for spectra containing underlying extra lines (e.g., due to ^{13}C) [9] or for spectral lines that overlap. Fitting the entire spectrum improves the precision by at least an order of magnitude [8]; however, the Voigt is time-consuming to calculate, thus there has been continuing interest in methods to approximate the absorption shape in many fields for many years [2, 10–13] continuing to the present [14]. For absorption spectra, a weighted sum of a Gaussian and a Lorentzian of the same line width and of unit peak-to-peak height, given by Eq. (5) of ref [8], is a particularly simple formulation as follows:

$$Y_{abs}^{sum'} = -V_{abs}^{fit}\left\{\eta_{abs}\frac{8\xi}{\left[3+\xi^2\right]^2} + (1-\eta_{abs})\xi\frac{\sqrt{e}}{2}e^{\frac{-\xi^2}{2}}\right\} \tag{2}$$

with $\xi = 2(H - H_0)/\Delta H_{pp}^{0}$ where, H and H_0 are the magnetic and the resonance fields, respectively; ΔH_{pp}^{0} is the peak-to-peak line width, common to both components; and V_{pp}^{fit} is the fit to the peak-to-peak intensity. The subscript *abs* denotes absorption, η_{abs} the fractional Lorentzian content and the prime reminds us that it is a first-derivative spectral line. An equivalent sum-function normalized to the doubly-integrated intensity is given by Eq. (6) of ref [8] and the conversion between the two formulations is given in the appendix of that reference. There is no *a priori* justification for Eq. (2); however, as detailed in ref [8], it is the same shape as the Voigt to within 0.5 % and a one-to-one map from the single parameter η_{abs} that defines the shape to the parameter χ may be formed. That is to say, given a value of the independent variable η_{abs}, a single value of the dependent variable χ may be obtained. Thus, the two important parameters, ΔH_{pp}^{G} and ΔH_{pp}^{L} are determined uniquely from the two measured parameters, η_{abs} and ΔH_{pp}^{0}. In principle, a map is required for each hyperfine pattern; however, these are similar for $\chi < 2$ to the precision detailed in section 5.1 of ref [6]. See p. 16 of ref [8] for a careful analysis of the fidelity of (2) when fit to a Voigt and Table 3 of that same reference for the map appropriate to the Voigt.

Most EPR spectra are measured as absorption spectra; thus, it's not surprising that little work [15–18] has been reported treating IHB dispersion spectra because there was no need. In recent years, the situation has changed because we know [19–27] that, as spectra are broadened by Heisenberg spin exchange and/or dipole-dipole interactions, dispersion components are introduced, producing admixtures of absorption and dispersion spectra. For Lorentzian

lines, the important parameter in these admixtures, in addition to ΔH_{pp}^{L}, is the ratio of the maximum intensity of the dispersion component and the peak-to-peak amplitude of the absorption component, V_{disp}/V_{pp}.

Unfortunately, the same strategy to develop a dispersion sum-function of form Eq. (2) is not straightforward, because there is no known analytical expression for the Gaussian component [5]. The purpose of this paper is to propose an accurate, simple analytical method to approximate the Gaussian dispersion component thus leading to a dispersion sum-function and, from this, a method to accurately analyze dispersion-absorption admixtures.

We undertook this work because it is sometimes needed to analyze nitroxide spectra; however, it might find use to analyze pure dispersion lines of Voigt form in other fields; for example, spectroscopic techniques that measure the interference between two or more light fields [5].

Theory IHB Dispersion

IHB Dispersion Manifolds

For nitroxides, there are, with very few exceptions 12 or more protons (deuterons) contributing hyperfine structure to the spectrum, often unresolved [6]. Magnet field modulation also contributes to IHB, but this may be considered separately [7]; thus, we develop the IHB dispersion profiles with manifolds consisting of Lorentzian dispersions imposed upon a hyperfine pattern. We base this development on the nitroxide 2,2,6,6-tetramethyl-4-oxopiperidine-1-oxyl (Tempone) with hyperfine coupling to $N = 12$ equivalent protons. Tempone was chosen because it is an ideal nitroxide to study experimentally being available commercially with either ^{14}N or ^{15}N; either deuterated or protonated;[2] very stable [25]; and soluble in a wide range of solvents [25, 28, 29]. It is well known that the binomial intensity pattern approximates a Gaussian profile [30]; thus, the Voigt is an excellent model of the shape of the spectra.

In this paper, we consider only one IHB manifold: in using the results to fit an experimental spectrum it is necessary to sum over all manifolds in the spectrum in order to account for line overlap as has been done for EPR spectra consisting of two (for ^{15}N) [22], three (for ^{14}N) [28], or five lines (for nitronyl-nitroxides) [21].

In general, for N equivalent protons, the pattern consists of N+1 lines spaced by $a > 0$ of binomial relative intensity given by

$$I_k = \frac{1}{2^N}\frac{N!}{(N-k)!k!} \qquad k = 0\ to\ N \tag{3}$$

[2] Sigma-Aldrich, Merck KGaA, Darmstadt, Germany.

From Eq. (19) of ref [19] a Lorentzian dispersion of unit maximum intensity and line width ΔH_{pp}^{L} is given as follows:

$$Y_{disp}^{L'} = 3\left(\frac{3-\xi_{Lk}^2}{\left[3+\xi_{Lk}^2\right]^2}\right) \tag{4}$$

where

$$\xi_{Lk} = 2\frac{H-H_{0k}}{\Delta H_{pp}^{L}} \tag{5}$$

where H is the magnetic field and H_{0k} the resonance field of the kth line given by H_{0k}=H_0+(k–N/2)a, where H_0 is the field at the center of the pattern. We simulate a dispersion manifold by imposing a Lorentzian on each line of the pattern and summing over the N+1 lines. For simplicity, we assume that the lines are of equal line width, ΔH_{pp}^{L}.

$$Y_{disp}^{man'} = V_{disp}\sum_{k=0}^{N}\frac{1}{2^N}\frac{N!}{(N-k)!k!}3\left(\frac{3-\xi_{Lk}^2}{\left[3+\xi_{Lk}^2\right]^2}\right) \tag{6}$$

where V_{disp} is the sum of the intensities of the Lorentzian components because $\sum_{k=0}^{N} N!/[(N-k)!k!] = 2^N$ [30]. In the absence of IHB; i.e., for $a = 0$, Eq. (6) reduces to a single Lorentzian dispersion of maximum intensity V_{disp}. For $a \neq 0$, denote by V_{disp}^{man} the maximum intensity of the manifold in Eq. (6).

From the second moment of the pattern, we may calculate ΔH_{pp}^{G} from a rearranged form of Eq. (2) of ref [6] as follows:

$$\Delta H_{pp}^{G} = a\sqrt{N\alpha} \tag{7}$$

where α is a parameter near unity that matches the line width of the pattern to that of a Gaussian of the same second moment [6]. Thus, from Eq. (1) the Voigt parameter is given by

$$\chi \equiv \frac{a\sqrt{N\alpha}}{\Delta H_{pp}^{L}} \tag{8}$$

The shape of the manifold is uniquely determined by χ so any combination of a and ΔH_{pp}^{L} satisfying Eq. (8) gives the same shape [6, 8].

For a Voigt, a relationship between ΔH_{pp}^{L}, ΔH_{pp}^{G} and ΔH_{pp}^{0} was given to an accuracy of 0.5 % by Dobryakov and Lebedev [31] as follows:

$$\left(\frac{\Delta H_{pp}^{G}}{\Delta H_{pp}^{0}}\right)^2 + \frac{\Delta H_{pp}^{L}}{\Delta H_{pp}^{0}} = 1 \tag{9a}$$

For Tempone, $N = 12$ and $\alpha = 1.08$ [6]. The bulk of the simulations employed a 10-G sweep width with a resolution of 0.01 G. For these, Eq. (9a) was exploited to determine combinations of a and ΔH_{pp}^{L} that yielded

Table 2 Input parameters to simulate Tempone dispersion and absorption manifolds

ΔH_{pp}^{L}, G	a, G	ΔH_{pp}^{G}, G[a]	χ[b]	ΔH_{pp}^{0}, G[c]
0.3940[d]	0.2730	0.9828	2.494	1.199
0.4200[d]	0.2690	0.9684	2.306	1.201
0.4680[d]	0.2600	0.9360	2.000	1.199
0.5770	0.2400	0.8640	1.497	1.199
0.7420	0.2060	0.7416	0.9995	1.200
0.7940	0.1940	0.6984	0.8796	1.200
0.9940	0.1380	0.4968	0.4998	1.200
1.110	0.09220	0.3319	0.2990	1.202

[a] Eq. (7)

[b] Eq.(8)

[c] Eq. (9a)

[d] Shows incipient resolution

the same value of ΔH_{pp}^{0} near 1.200 G. Table 2 gives the input parameters for the simulations that were carried out with a commercial program Kaleidagraph (2457 PERKIOMEN AVE.READING, PA 19606) in double precision, which is accurate to 16 digits, and fit using the Levenberg-Marquardt algorithm in its library. Other combinations of a, ΔH_{pp}^{L}, sweep widths, and resolutions were also employed to confirm the results. For convenience, in the text and in the rest of the tables, we refer to χ rounded to two places; for example, we call $\chi = 2.494$, $\chi = 2.5$, etc.

Dispersion Sum-Function

We seek to approximate a dispersion manifold as a sum of Lorentzian and Gaussian components analogous to Eq. (2):

$$Y_{disp}^{sum'} = V_{disp}^{fit}\left[\eta_{disp} Y_{disp}^{L'}(\xi) + \left(1-\eta_{disp}\right) Y_{disp}^{G'}(\xi)\right] \tag{10}$$

where V_{disp}^{fit} is the fit to the maximum intensity; $Y_{D}^{L'}(\xi)$ and $Y_{D}^{G'}(\xi)$ are Lorentzian and Gaussian dispersion shapes of unit maximum intensities, respectively; and η_{disp} is the Lorentzian character. The Lorentzian component of Eq. (10) is of the form of Eq. (4), however, with line width ΔH_{pp}^{0} as follows:

$$Y_{disp}^{L'}(\xi) = 3\left(\frac{3-\xi^2}{\left[3+\xi^2\right]^2}\right) \tag{11}$$

where

$$\xi = \frac{2(H-H_0)}{\Delta H_{pp}^{0}} \tag{12}$$

In search of a form for $Y_{disp}^{G'}(\xi)$, we began by noting that Eq. (11) is similar in form to the derivative of the Lorentzian absorption, the first term in the brackets of Eq. (2). In fact, Eq. (11) is given by that derivative multiplied by a rational fraction. Therefore, we began by examining the derivative of $Y_{abs}^{G'} = \sqrt{e}\xi e^{-\xi^2/2}/2$, which yields

$$\frac{dY_{abs}^{G'}}{d\xi} = \frac{\sqrt{e}}{2} e^{\frac{-\xi^2}{2}}\left[1-\xi^2\right] \tag{13}$$

First, we searched for an approximate form as a product of Eq. (13) and a rational fraction, but had no success. Next, we tried a simpler form as follows:

$$Y_{disp}^{G'}(\xi) \propto e^{\frac{-\xi^2}{2}} P_{even}(\xi) \tag{14}$$

where $P_{even}(\xi)$ is an even-order polynomial. Fortunately, we found that Eq. (13) already improves the fit considerably and that the simplest extension of Eq. (13) imaginable provides satisfactory fits to the dispersion manifolds as follows:

$$Y_{disp}^{G'}(\xi) = e^{\frac{-\xi^2}{2}}\left[1-\xi^2-\varepsilon(\chi)\cdot\xi^4\right] \tag{15}$$

Fortuitously, the coefficient $\varepsilon(\chi)$ turns out to be rather constant, especially in the range of $\chi = 2.5$–0.5 where accounting for the Gaussian component is needed the most. In this range, fitting the manifolds in Table 2 to Eq. (10) utilizing Eq. (15); fixing ΔH_{pp}^{0} at its known value; and allowing $\varepsilon(\xi)$, V_{disp}^{Sum}; and η_{disp} to vary as adjustable parameters yields $\varepsilon(\xi) = 0.272 \pm 0.007$ as the mean value and standard deviation over the 6 manifolds. Using a constant value of 0.27 obviates the need for an additional adjustable parameter; therefore, we propose and test the following form:

$$Y_{disp}^{sum'} = V_{disp}^{Sum}\left\{\eta_{disp}\frac{3\left(3-\xi^2\right)}{\left(3+\xi^2\right)^2} + \left(1-\eta_{disp}\right)e^{\frac{-\xi^2}{2}}\left[1-0.27\cdot\xi^4\right]\right\}. \tag{16}$$

Equation (16) cannot be justified from first principles. Its justification is the same as that for Eq. (2): it is accurate for all values of $\chi < 2.5$ as detailed in Table 3 of the next section and the mixing parameters, η_{disp}, may be uniquely mapped to known input parameters.

Many expressions more complicated than Eq. (16), some involving a linear term (as the principal square root of ξ^2), were found that reduced the global least-squares; however, they all recovered less accurate values of the parameters of interest, V_{man}^{disp} and ΔH_{pp}^{L}.

Results IHB Dispersion

Figure 1a shows the individual Lorentzian dispersions of a manifold for $\chi = 2.5$ and Fig. 1b, the sum, Eq. (6). The manifold is unresolved in the sense that no distinct lines may be perceived visually; however, incipient resolution is apparent as seen near the center of the line. For Tempone, judging absorption spectra visually, a value of χ marking

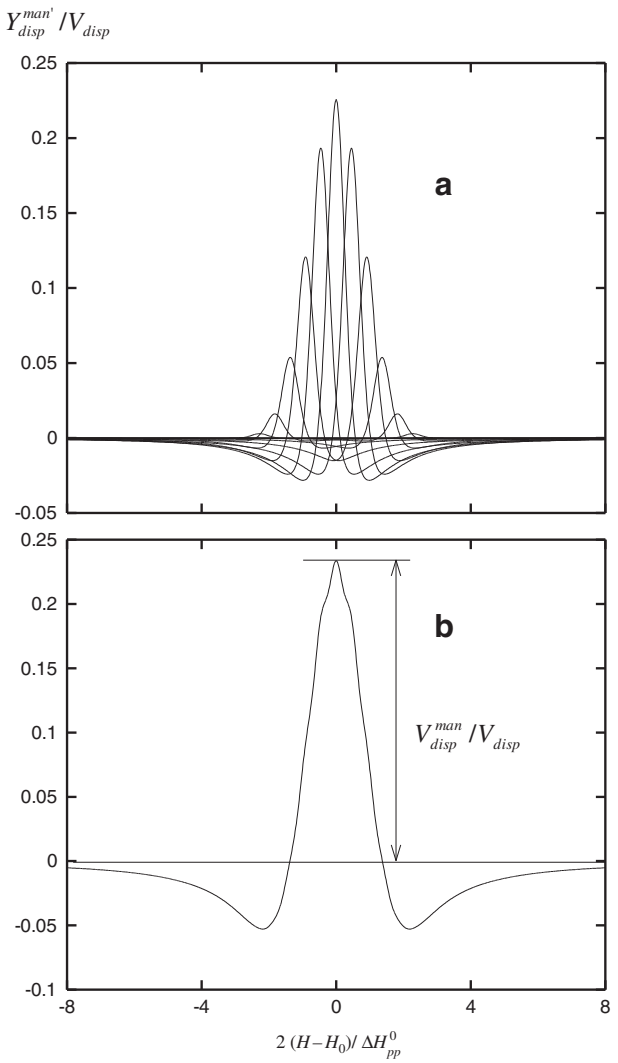

Fig. 1 **a** Thirteen Lorentzian dispersions of binomial relative intensities of width $\Delta H^L_{pp} = 0.394\,G$, spaced by $a = 0.273$ G. On this scale, there appear to be 9 lines because the outer 4 are not observable. **b** The manifold given by the sum of the components, Eq. (6). The maximum value of the manifold, $V^{man}_{disp}/V_{disp} = 0.2337$, is shown. An identical figure results from multiplying both ΔH^L_{pp} and a by positive number

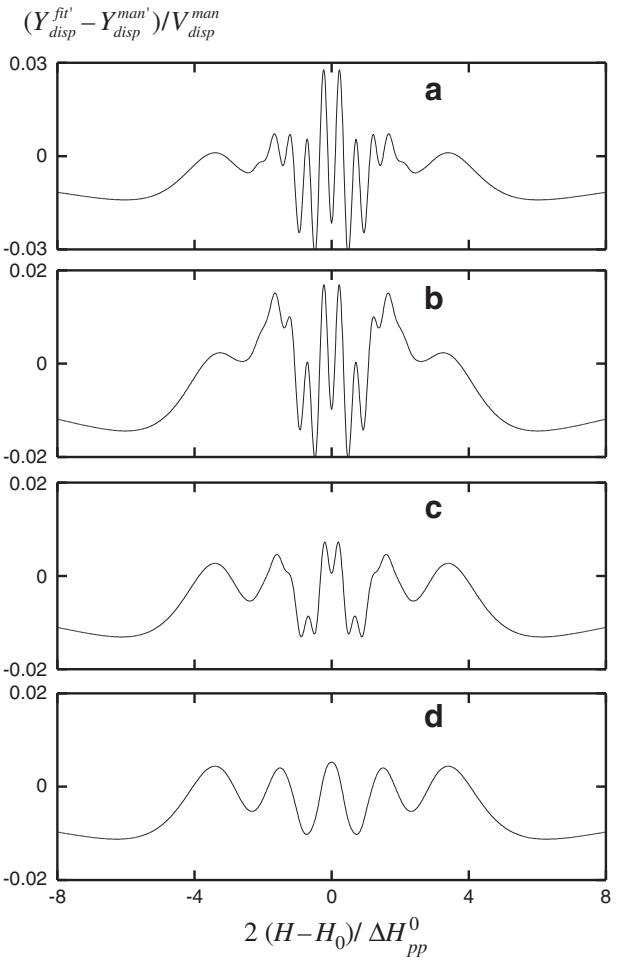

Fig. 2 Residuals as a fraction of V^{man}_{disp} at: **a** $\chi = 2.5$; **b** $\chi = 2.3$; **c** $\chi = 2.0$; and **d** $\chi = 1.5$. Note that the scale of the ordinate in **a** is 50 % larger than in the others. The residuals for smaller values of χ are similar to **d** but with decreasing amplitude

the onset of incipient resolution was reported as $\chi_{inc} = 2.3$ [6]; however, the value of χ_{inc} using that criterion is clearly subjective. A clearer determination of χ_{inc} emerges from fitting the manifolds as shown in Fig. 2 below.

Figure 3 shows dispersion manifolds for $\chi = 0$, (a); 0.5, (b); 1.0, (c); 1.5, (d); and 2.5, (e) respectively. V^{man}_{disp}/V_{disp} varies from unity for the Lorentzian, $\chi = 0$, to 0.2337 for $\chi = 2.5$. The ordinate is offset for clarity by the amounts: (a), 0; (b) −0.04; (c) −0.08; (d) −0.12; and (e) −0.17, respectively. The positions of the minima move toward the center of the manifold as χ increases. Although difficult to judge from Fig. 3, the minima become relatively more pronounced as χ increases.

Figure 4a displays a $\chi = 2.0$ manifold (solid line) together with a least-squares fit (dashed line) to a Lorentzian dispersion, Eq. (11). Figure 4b shows the residuals from the fit as a fraction of the maximum intensity, $Y^{man'}_{disp}/V^{man}_{disp}$. The maximum deviation, occurring near 2 half-widths, is 9.9 %.

Figure 5a shows the same $\chi = 2.0$ manifold together with a least-squares fit (dashed line) to Eq. (16). Comparison with Fig. 4a shows a rather dramatic improvement in the fit by including a Gaussian component. Figure 5b shows the residuals on a scale 5 times smaller than that of Fig. 3b. Visual inspection of Fig. 5a shows little hint of incipient resolution; however, it can be perceived as the narrow residuals near the center of Fig. 5b. The maximum deviation, occurring near 6 half-widths from the center, is −1.3 %.

Results from fits to Eq. (11) and Eq. (16) are given in Table 3. The errors using a Lorentzian only fit, Eq. (11), are substantial: V^{man}_{disp}/V_{disp} is in error averaging 6.5 % from $\chi = 2.5$–0.880, 2.6 % at $\chi = 0.500$, and 1.2 % at $\chi = 0.3$. The

Table 3 Parameters from fits of dispersion manifolds to Eq. (11) or Eq. (16)

χ	V_{disp}^{man}/V_{disp} [a]	V_{disp}^{fit}/V_{disp}		$\Delta H_{pp}^{fit}/\Delta H_{pp}^{0}$		η_{disp}	Maximum Deviation[b]	
		Eq. (11)	Eq. (16)	Eq. (11)	Eq. (16)	Eq. (16)	Eq. (11)	Eq. (16)
2.50[c]	0.2337	0.2481	0.2287	0.8275	1.013	0.8228	10 %	−3.2 %
2.3[c]	0.2562	0.2746	0.2537	0.8316	1.013	0.8280	9.9	−2.2
2.00[c]	0.3008	0.3244	0.3010	0.8417	1.011	0.8377	9.3	−1.3
1.50	0.4103	0.4400	0.4124	0.8550	1.010	0.8601	7.7	−1.1
0.999	0.5808	0.6130	0.5837	0.8850	1.007	0.8953	5.5	−0.8
0.880	0.6337	0.6650	0.6366	0.8958	1.006	0.9068	4.9	−0.7
0.500	0.8268	0.8483	0.8294	0.9408	1.002	0.9523	2.6	−0.4
0.300	0.9265	0.9373	0.9281	0.9742	1.002	0.9788	1.2	−0.2

[a] Directly measured from manifolds. Fig. 1b

[b] Maximum residual as a percentage of V_{disp}^{man}

[c] Shows incipient resolution

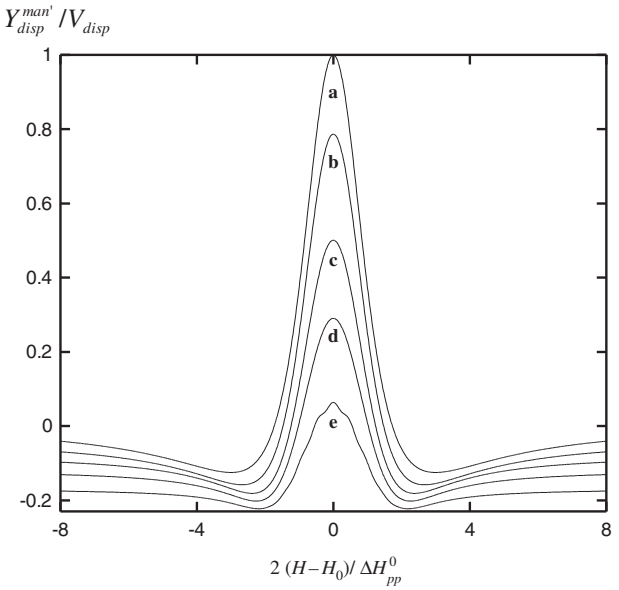

Fig. 3 Dispersion manifolds for $\chi = 0$, **a**; 0.5, **b**; 1.0, **c**; 1.5, **d**; and 2.5, **e**. V_{disp}^{man}/V_{disp} varies from unity for the Lorentzian, $\chi = 0$, to 0.2337 for $\chi = 2.5$. The ordinate is offset for clarity. See text. The depths of the minima become relatively more pronounced and the positions of the minima move toward the center of the manifold as χ increases

line width is poorly recovered: $\Delta H_{pp}^{fit}/\Delta H_{pp}^{0}$ is in error 17 % at $\chi = 2.5$, averaging 14 % from $\chi = 2.5$–0.880, 5.9 % at $\chi = 0.500$, and 2.6 % at $\chi = 0.3$.

Adding the Gaussian component in Eq. (16) improves the results considerably: V_{disp}^{man}/V_{disp} is in error by 2.1 % at $\chi = 2.5$, 1.1 % at $\chi = 2.3$, and less than 0.5 % for $\chi < 2.00$. $\Delta H_{pp}^{fit}/\Delta H_{pp}^{0}$ is in error by 1.3–1.1 % for $\chi = 2.5$–2.0 and less than 1 % for $\chi < 2.00$. Keeping in mind that the manifolds for $\chi = 2.5$–2.0 show incipient resolution, the agreement is excellent. The final two columns of Table 3 give the maximum deviations. The positions of the maximum discrepancies from fits to Eq. (16) are well away from the manifold, 5–6 half-line widths, while those from fits to Eq. (11) are closer, about 2 half-line widths. RMS values of the residuals (not shown) are a factor of 3–5 larger for the Lorentzian-only fit.

Figure 2 shows residuals using Eq. (16) as follows: (a) $\chi = 2.5$, (b) $\chi = 2.3$, (c) $\chi = 2.0$, and (d) $\chi = 1.5$. Note that the scale in (a) is 50 % larger than those in (c)–(d). The narrow residuals in the central part of the spectrum, due to incipient resolution, disappear for $\chi < 2.0$ giving a clearer criterion to define the value of χ_{inc}. The form of the residuals for values of $\chi < 1.5$ is similar to that in (d) with amplitudes that decrease with χ. Table 3.

For pure dispersions manifolds, χ and η_{disp} form the map to separate ΔH_{pp}^{G} and ΔH_{pp}^{L} employing Eqs. (9b) and (1).

Theory IHB Absorption Manifolds

From Eq. (19) of ref [19] a Lorentzian absorption of unit maximum intensity and line width ΔH_{pp}^{L} is given as follows:

$$-8\left(\frac{\xi_{Lk}}{\left[3+\xi_{Lk}^{2}\right]^{2}}\right) \tag{17}$$

with the same definitions as those following Eq. (5). Therefore, an absorption manifold is constructed as follows:

$$Y_{pp}^{man'} = -V_{pp}\sum_{k=0}^{N}\frac{1}{2^{N}}\frac{N!}{(N-k)!k!}8\left(\frac{\xi_{Lk}}{\left[3+\xi_{Lk}^{2}\right]^{2}}\right) \tag{18}$$

Where V_{pp} is the sum of the peak-to-peak intensities of the Lorentzian components; i.e., the intensity of the

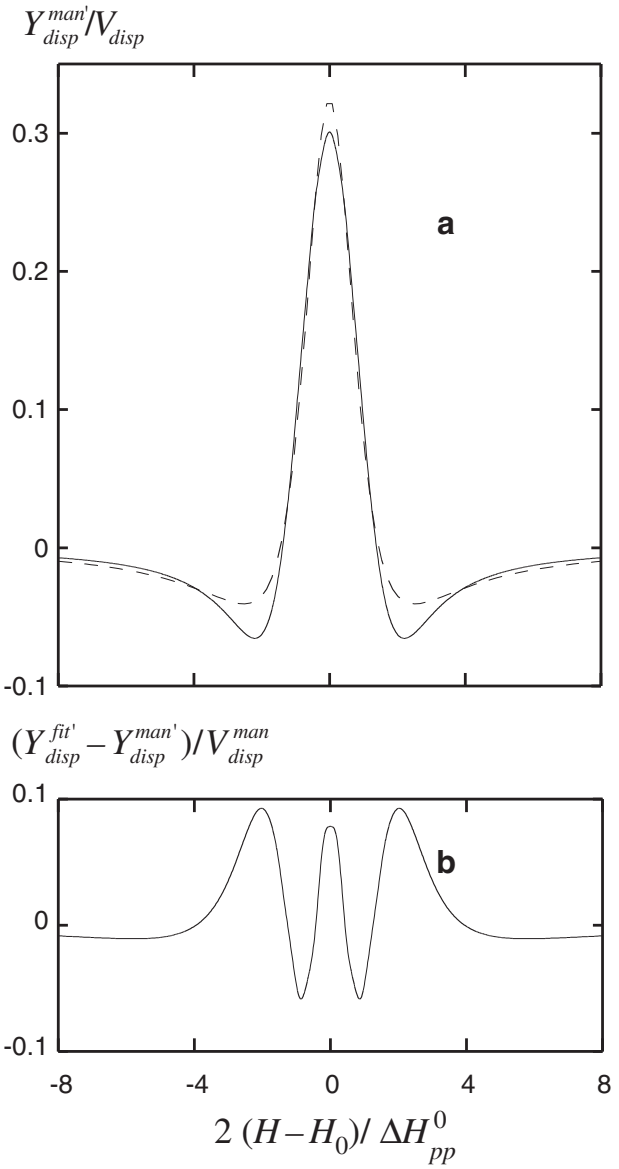

Fig. 4 **a** Dispersion manifold for $\chi = 2$, solid line, and best fit to a simple Lorentzian, Eq. (11), dashed line. **b** The residual as a fraction of the maximum amplitude, V_{disp}^{man}. The maximum residual, 9.3 %, occurs at approximately two half-widths from resonance

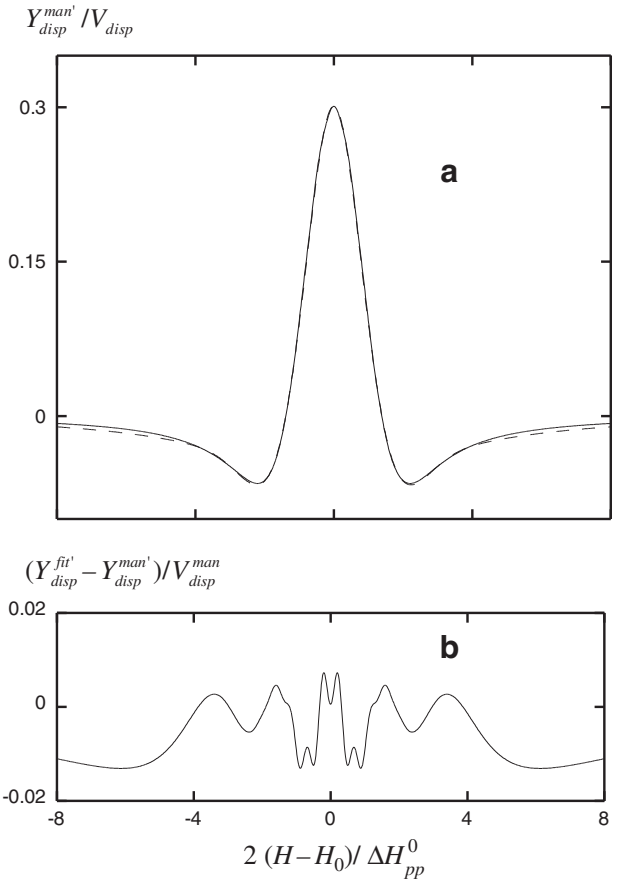

Fig. 5 **a** Manifold for $\chi = 2$, solid line, and best fit to Eq. (16), dashed line. **b** The residual as a fraction of the maximum amplitude; i.e., $\left(Y_{disp}^{fit'} - Y_{disp}^{man'}\right)/V_{disp}^{man}$. Note that the scale of Fig. 4b is five times larger than that in this figure. The maximum residual, −1.3 %, occurs at approximately 6 half-widths from resonance. Note the narrow-line structure near the center

resulting Lorentzian for $a = 0$. For $a > 0$, denote the peak-to-peak intensity of the manifold in Eq. (18) by V_{pp}^{man}. The absorption manifolds were computed with the same input parameters given in Table 2.

Results IHB Absorption

Figure 6a shows the individual Lorentzian absorptions of a manifold for $\chi = 2.5$ and Fig. 6b, the sum, Eq. (18), with the peak-to-peak intensity, V_{pp}^{man}/V_{pp}, defined. Incipient resolution is apparent as seen near the center of the line.

Figure 7a shows the absorption manifold for $\chi = 2$, solid line, and best fit to Eq. (2), dashed line, which is barely perceptible on this scale. Figure 7b displays the residuals as a fraction of $Y_{pp}^{man'}/V_{pp}$. Note that the scale of Fig. 7b is 6.7 times smaller than that of Fig. 5b. Even for this spectrum, showing slight incipient resolution by the narrow components near the center of Fig. 7b, the maximum residual is only 0.33 % occurring at approximately 6 half-widths from resonance. Equation (2) is credited [8, 31] with fitting the Voigt to an accuracy of 0.5 %; for this manifold, the fit is slightly better than that. Clearly the absorption manifold is fit more precisely by Eq. (2) than is the dispersion manifold by Eq. (16). Fitting all of the manifolds to Eq. (2) reproduces values of ΔH_{pp}^{fit} that are within 0.4 % of the values of ΔH_{pp}^{0} computed from Eq. (9a), last column of Table 2.

The results of fits of absorption manifolds to Eq. (2) are given in Table 4. The first two columns define the map from η_{abs} to χ as shown in Fig. 8, circles. To analyze an unknown spectrum, it is fit to Eq. (2) that yields values of η_{abs} and

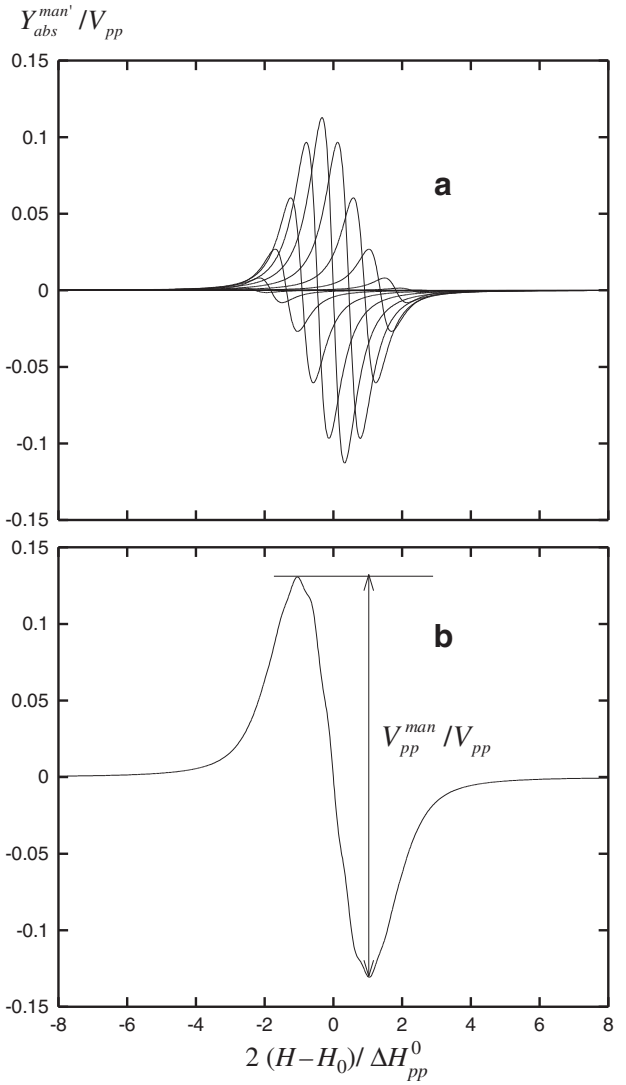

Fig. 6 **a** Thirteen Lorentzian absorptions of binomial relative intensities of width $\Delta H_{pp}^L = 0.394\,G$, spaced by $a = 0.273$ G. On this scale, there appear to be 9 lines because the outer 4 are not observable. **b** The manifold given by the sum of the components. The peak-to-peak intensity, V_{pp}^{man}/V_{pp}, is shown

ΔH_{pp}^0 from which the map in Fig. 8 yields the value of χ. The analysis is completed from Eq. (9a) rearranged as follows:

$$\Delta H_{pp}^L = \frac{\Delta H_{pp}^0\left(-1+\sqrt{1+4\chi^2}\right)}{(2\chi^2)} \tag{9b}$$

and ΔH_{pp}^G follows from Eq. (1). As the value of χ approaches zero, the value of ΔH_{pp}^G becomes small and, as a percentage, less certain.

The map may be utilized to interpolate between measured values of η_{abs}; however, for most cases sufficient accuracy may be obtained using the following rational

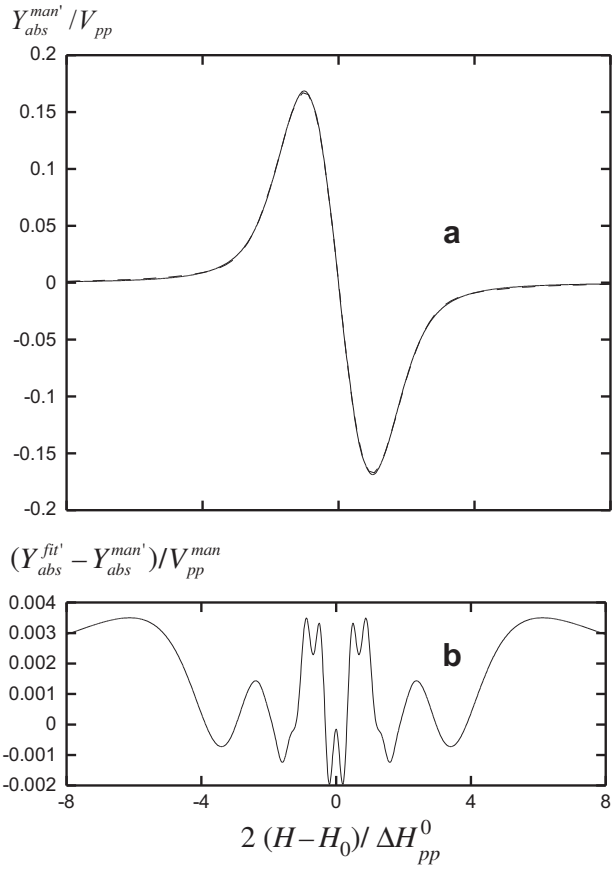

Fig. 7 **a** Absorption manifold for $\chi = 2$, solid line, and best fit to Eq. (2), dashed line. **b** The residual as a fraction of V_{pp}^{man} on a scale 6.7 times smaller than that of Fig. 5b. The maximum residual, −0.33 %, occurs at approximately 6 half-widths from resonance. Note the narrow-line structure near the center

fraction:

$$\chi = \frac{0.36 - 0.266\eta_{abs}^2}{0.0286 + 0.48\eta_{abs}} \tag{19}$$

Equation (19) is plotted as the solid line in Fig. 8. Using Eq. (19) rather than an interpolation leads to an error in ΔH_{pp}^L of 1.1 % at $\chi = 2.5$ and less than 0.6 % everywhere else. The squares in Fig. 8, almost coincident with the circles, are derived from absorption-dispersion admixtures, the next section.

Theory Absorption–Dispersion Manifold Admixtures

Unwanted absorption-dispersion admixtures are observed in EPR. There are techniques to minimize the dispersion [32] and methods to correct for its presence [11]. For nitroxides undergoing spin exchange and/or dipole-dipole interactions, the admixtures occur for perfectly balanced bridges and are very much wanted because they provide a valuable tool in

Table 4 Parameters from fits of absorption manifolds to Eq. (2). Tempone map

χ	η_{abs}	$\Delta H_{pp}^{fit}/\Delta H_{pp}^{0}$ [a]	V_{pp}^{fit}/V_{pp} [a]	$\Delta H_{pp}^{man}/\Delta H_{pp}^{0}$ [b]	V_{pp}^{man}/V_{pp} [b]
2.50[c]	0.2324	0.9997	0.2569	1.046	0.2614
2.30[c]	0.2533	1.000	0.2841	1.032	0.2875
2.00[c]	0.2921	0.9986	0.3349	1.010	0.3373
1.50	0.3838	0.9980	0.4524	0.9980	0.4545
1.00	0.5321	0.9974	0.6257	0.9953	0.6285
0.880	0.5814	0.9972	0.6774	0.9947	0.6802
0.500	0.7821	0.9963	0.8564	0.9933	0.8587
0.300	0.9024	0.9991	0.9414	0.9973	0.9426

[a] Fits to Eq. (2)

[b] Directly measured from manifolds. Fig. 6b

[c] Shows incipient resolution

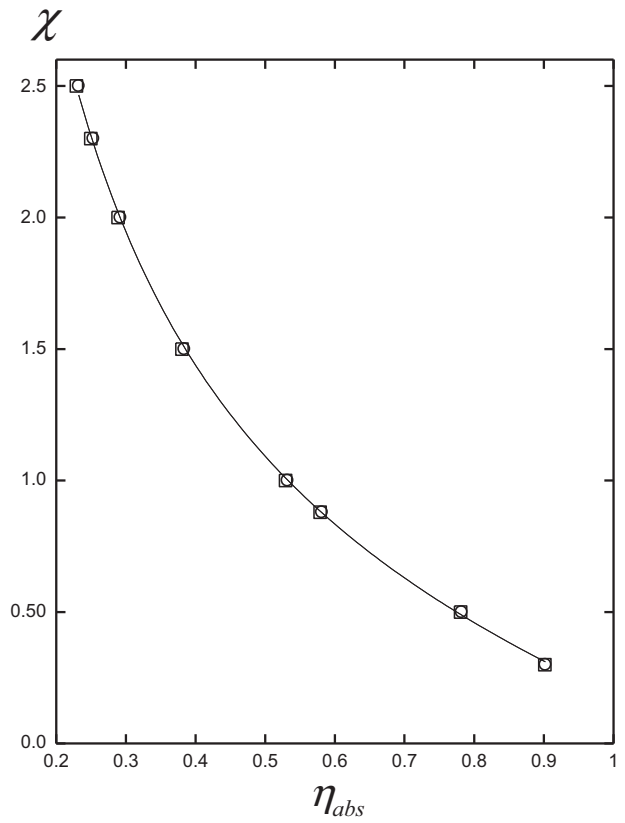

Fig. 8 Map from η_{abs} to χ, circles. Results from fitting admixtures to Eq. (20) with $V_{disp}/V_{pp} = 0.300$, squares. Solid line, Eq. (19)

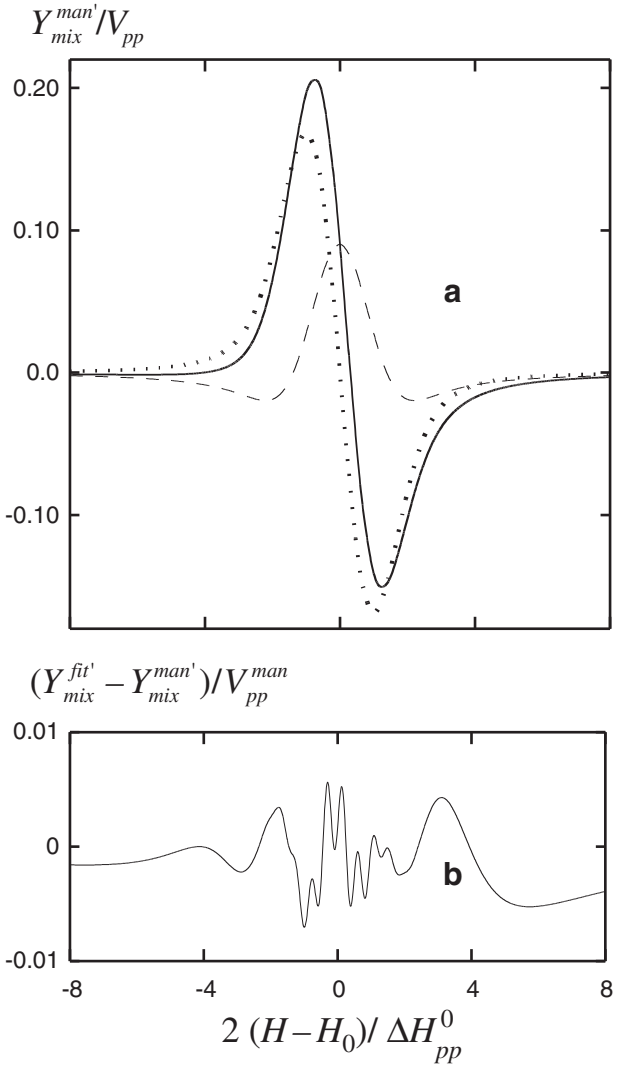

Fig. 9 **a** Dispersion manifold, dashed, absorption manifold, dotted, and the admixture, solid line, for an input Lorentzian ratio $V_{disp}/V_{pp} = 0.300$ and $\chi = 2.0$, normalized to V_{pp}. On this scale, the fit to Eq. (20) is indistinguishable from the admixture. **b** The residual as a fraction of the peak-to-peak intensity of the admixture

interpreting the data [26]. Whether the dispersion is wanted or not, it is useful to separate it from the absorption component of the admixture post experiment.

Absorption–dispersion admixtures may be constructed by adding the patterns like those in Figs. 1a and 6a scaled by a given relative intensity, V_{disp}/V_{pp}. Thus, each Lorentzian line in the pattern has the same value of V_{disp}/V_{pp}, so the average value of V_{disp}/V_{pp} is well defined.

We next investigate how well admixtures may be fit with the following:

$$Y_{mix}^{sum'} = Y_{disp}^{sum'} + Y_{abs}^{sum'}. \quad (20)$$

where $Y_{disp}^{sum'}$ is given by Eq. (16) and $Y_{abp}^{sum'}$ by Eq. (2).

Results Absorption–Dispersion manifold admixtures

The solid line in Fig. 9a shows a mixture of absorption and dispersion manifolds at an input Lorentzian ratio $V_{disp}/V_{pp} = 0.300$ for $\chi = 2.0$. The dashed line displays the dispersion

and the dotted, the absorption. Figure 9b displays the residual as a fraction of the peak-to-peak intensity of the mixture showing that the maximum discrepancy is 0.7 %; therefore, the admixture is well fit. Table 5 gives the parameters from fits to Eq. (20). The third and fourth columns give values of $\Delta H_{pp}^{fit}/\Delta H_{pp}^{0}$ as fit to the admixture by Eq. (20) or fit to the absorption manifolds only by Eq. (2) showing that the discrepancies are utterly negligible. Similarly, the fifth and sixth columns show values of $V_{disp}^{fit}/V_{pp}^{fit}$ from fits to the admixtures or to separate manifolds, respectively. The discrepancy in these values is 0.7 % at $\chi = 2.5$ and 2.3 and less than 0.5 % elsewhere. The values of η_{abs} determined from fits to Eq. (20) in Table 5 are plotted (squares) in Fig. 8 together with correct map, circles. These discrepancies in η_{abs} lead to an error in ΔH_{pp}^{L} of 1.1 % at $\chi = 2.5$ and less than 1 % everywhere else and an error in ΔH_{pp}^{G} of 0.4 % at all values of χ.

Therefore, the parameters are well recovered. The implication of this is that one may begin with an admixture and recover the absorption and dispersion components separately. A plot of the fit to the absorption component alone and that component recovered from the admixture overlay almost exactly and the same is true of the dispersion, so plots of these are not shown; rather, Fig. 10 shows the residuals from fits to the $\chi = 1.5$ dispersion and absorption components separately, the solid lines, and the fits of a $V_{disp}/V_{pp} = 0.300$ admixture. Clearly, the only significant discrepancies are due to the approximations inherent in Eqs. (2) and (18), additional discrepancies introduced by Eq. (20) are negligible.

As can be observed in Fig. 9a, admixtures result in asymmetric spectra and shift the field at which the spectrum crosses the baseline. The low-field line of a nitroxide broadened by spin exchange is similar to that in Fig. 9a. Because the dispersion component is of opposite sign for

Table 5 Parameters from fits of dispersion-absorption admixtures[a]

χ	η_{abs} [a]	$\Delta H_{pp}^{fit}/\Delta H_{pp}^{0}$ [a]	$V_{disp}^{fit}/V_{pp}^{fit}$ [a]	$V_{dis}^{fit}/V_{pp}^{fit}$ [b]	$V_{dis}^{man}/V_{pp}^{man}$ [c]
2.50[d]	0.2290	1.001	0.8963	0.8901	0.8940
2.30[d]	0.2499	1.002	0.8991	0.8931	0.8913
2.00[d]	0.2888	1.000	0.9044	0.8986	0.8918
1.50	0.3807	0.9994	0.9168	0.9117	0.9027
1.00	0.5294	0.9985	0.9368	0.9328	0.9241
0.880	0.5788	0.9983	0.9434	0.9398	0.9316
0.500	0.7804	0.9969	0.9706	0.9685	0.9629
0.300	0.9016	0.9994	0.9868	0.9859	0.9829

[a] Fits to Eq. (20) for $V_{disp}/V_{pp} = 0.300$

[b] Ratio of fits of the dispersion manifolds to Eq. (16) and of the absorption manifolds to Eq. (2)

[c] Ratio of directly measured V_{dis}^{man} from dispersion manifolds and V_{pp}^{man} from absorption manifolds

[d] Shows incipient resolution

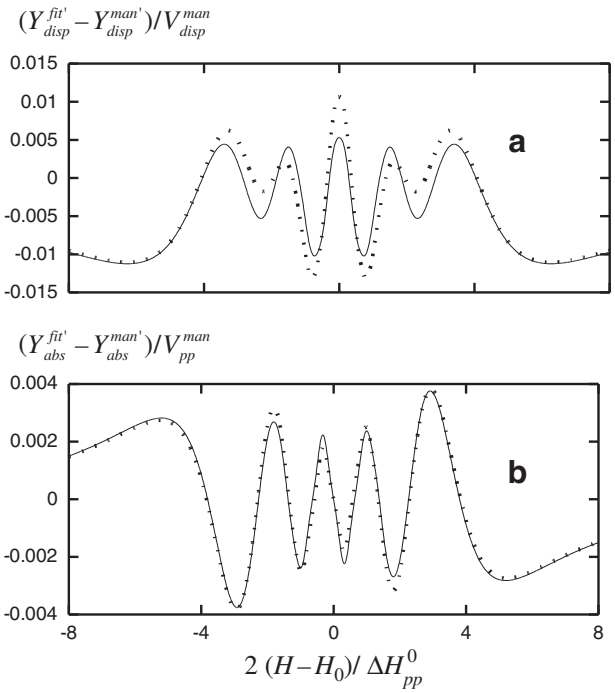

Fig. 10 **a** The solid line shows residuals from the fit of the $\chi = 1.5$ dispersion manifold to Eq. (16). The dotted line gives the residuals when a $V_{disp}/V_{pp} = 0.300$ admixture is fit to Eq. (20). The maximum residual is increased marginally, from 1.3 % to 1.4 % **b** Residuals from fits of the $\chi = 1.5$ absorption manifold to Eq. (2), solid line, or an admixture, Eq. (20), dotted line. Note that the scale in **a** is 3.75 times larger than that in **b**

the high-field line, that asymmetry is opposite. See Fig. 4 of ref [26] for simulated spectra and Fig. 3 of ref [19] for an experimental spectrum.

Both V_{disp}^{man} and V_{pp}^{man} decrease as χ increases, but they decrease at different rates, so the task is to relate the measured $V_{disp}^{fit}/V_{pp}^{fit}$ to the desired intrinsic value V_{disp}/V_{pp}. Table 3 was compiled by fitting admixtures with $V_{disp}/V_{pp} = 0.300$ to illustrate, but $V_{disp}^{fit}/V_{pp}^{fit}$ varies linearly ($r = 1.000$) with V_{disp}/V_{pp}, so.

$$\frac{V_{disp}^{fit}}{V_{pp}^{fit}} = \theta(\chi) \cdot \frac{V_{disp}}{V_{pp}}. \tag{21}$$

for all V_{disp}/V_{pp}, where the left-hand side is found from fits to Eq. (20). The 5th column of Table 5 tabulates $\theta(\chi)$ while the last two columns were found using fits to Eq. (2) and Eq. (16) separately, respectively which differ by less than 1 % at all values of χ. From a fit value of $V_{disp}^{fit}/V_{pp}^{fit}$, Table 5 may be used to interpolate to obtain a value of V_{disp}/V_{pp}, or the following approximation gives the result to within 0.6 %:

$$\theta(\chi) = 1 - 0.074\chi + 0.0127\chi^2 \tag{22}$$

The only parameter that varies significantly as a function of V_{disp}/V_{pp} is η_{abs}. This results in discrepancies in χ of

1.5–1.1 % for $\chi = 2.5$–2.0 and less than 1 % elsewhere. From Eq. (9b), we find that these discrepancies yield errors in ΔH^L_{pp} that reach 3.6, 2.7, and 1.7 % at $V_{disp}/V_{pp} = 1$ for $\chi = 2.0$, 1.5 and 1.0, respectively. For $V_{disp}/V_{pp} < 0.4$, the discrepancies in ΔH^L_{pp} are 1 % for all χ.

Effect of Noise on Absorption–Dispersion Admixtures

Figure 10 shows the same admixture in Fig. 9a with added noise (percent of peak-to-peak intensity) (a) 3 %, (b) 10 %, (c) 40 %, and fits to Eq. (20), circles. The noise was generated using the random number generator of Kaleidagraph. (c) Shows the residue of the 10 % noise spectrum showing no systematic difference between the spectrum and fit. The Levenberg-Marquardt algorithm is surprisingly robust in finding fits of Eq. (20) to spectra such as those in Fig. 9d as long reasonable first estimates are employed.

To replicate a typical experimental protocol [28], spectra were generated 5 times and fit. From the results, the mean values and standard deviations of the parameters were computed and displayed in Table 6. At all noise levels, all of the correct parameters are found well within the standard deviations. At 3 % noise, all parameters are with 1 % of the correct values. The errors in the mean value of ΔH^{fit}_{pp} are negligible except at 40 % noise where it is 2 %. The error in ΔH^L_{pp} is 1 % and 9 % for noise levels of 10 and 40 %, respectively. $V^{fit}_{disp}/V^{fit}_{pp}$ is in error by 1.5 % or less.

Effect of Extraneous lines

Early efforts to separate ΔH^L_{pp} and ΔH^G_{pp} employed measures at a few points on the spectrum rather than fits [6]. In addition to losing valuable line shape information and the ability to handle noise, a problem could arise when extraneous lines are mixed with the admixture. A common example of this is caused by hyperfine lines due to ^{13}C in natural abundance [9]. For this case, one may usually correct for their presence [9]; however, what about the case in which does not know about such a line? The possibilities are endless, so we briefly investigate the problem with an example of an extraneous Lorentzian line from a species with a relative concentration that is 3 % of that of the species yielding the admixture. We assume that the line width of the extraneous line is 40 % of ΔH^0_{pp} for the admixture. Figure 11a shows the extraneous line and 11b the superposition of it and the admixture in Fig. 9a. The fit to Eq. (20) is shown by the dashed line and Fig. 11c the residual. The baselines of both the extraneous line and the residual are offset for clarity. The results on the parameters of the admixture are given in the last row of Table 6. Comparing these values with those in the first

Table 6 Results of Fitting an Admixture with Added noise or an Extraneous line to Eq. (20)[a]

Noise, %	$\Delta H^{fit}_{pp}/\Delta H^0_{pp}$	$\Delta H^L_{pp}(fit)/\Delta H^L_{pp}$	$V^{fit}_{disp}/V^{fit}_{pp}$
0	1.000	0.993	0.9043
3[b]	1.000 ± 0.002	0.999 ± 0.024	0.9032 ± 0.0013
10[b]	0.998 ± 0.005	1.01 ± 0.04	0.918 ± 0.010
40[b]	1.02 ± 0.03	0.91 ± 0.21	0.090 ± 0.036
0[c]	1.03	0.906	0.976

[a] $\chi = 2.00$, $V_{disp}/V_{pp} = 0.300$

[b] Mean values and standard deviation of 5 simulations and fits

[c] Added extraneous Lorentzian line with line width 0.4 ΔH^0_{pp} and doubly-integrated intensity 3 % of admixture. Fig. 11a

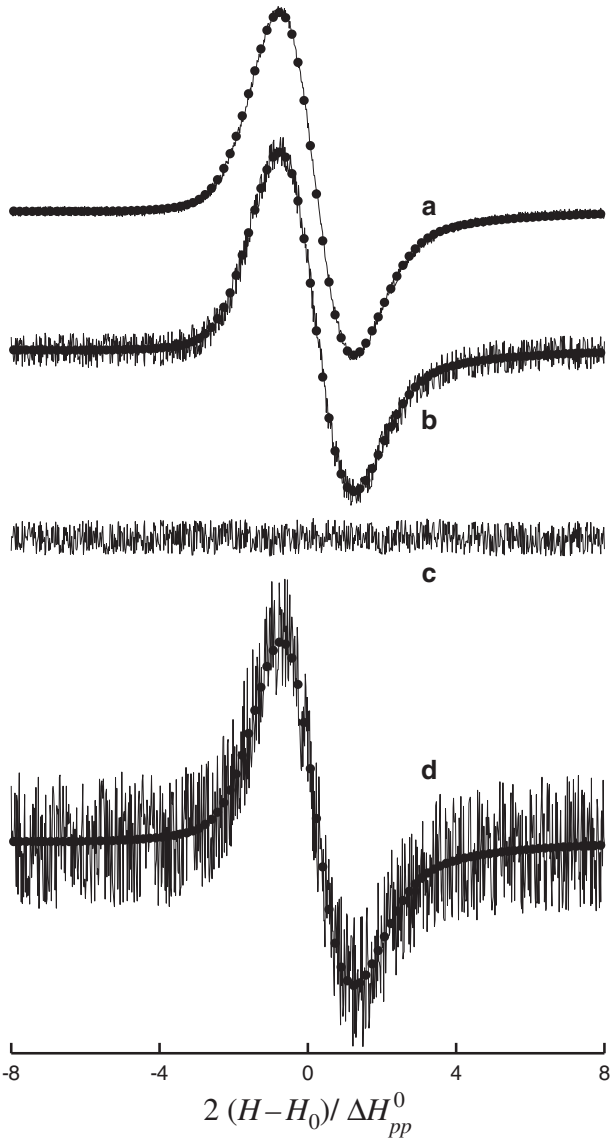

Fig. 11 Spectrum of Fig. 9a with added noise (% of peak-to-peak intensity). **a** 3 %, **b** 10 %, and **d** 40 %. **c** Residual of **b**. The spectrum, including noise, is fit to Eq. (20), the fit shown by, filled circles, every 10th datum. Each time such a spectrum is generated, the fit is different because the random noise is different

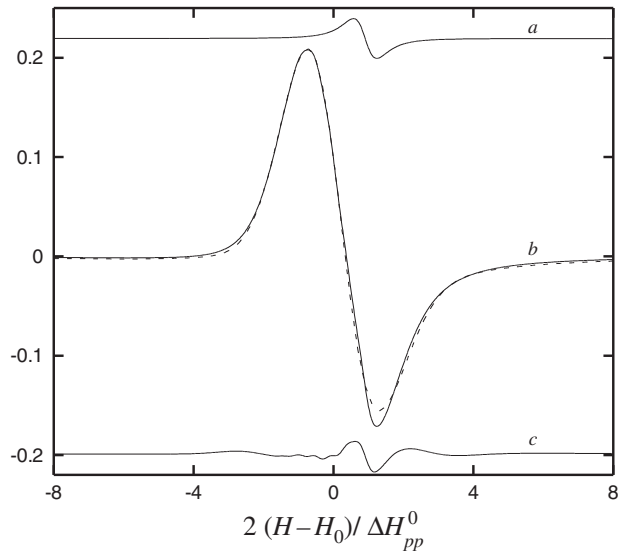

Fig. 12 **a** An extraneous Lorentzian line of width 0.4 and doubly-integrated intensity 3 % of that of the admixture in Fig. 9a. **b** The sum of the extraneous line in **a** and the admixture, solid line, and the fit to Eq. (20), dotted line. **c** The residual

row shows that consider errors are incurred: 3 % for $\Delta H_{pp}^{fit}/\Delta H_{pp}^{0}$, 9.4 % for $\Delta H_{pp}^{L}(fit)/\Delta H_{pp}^{L}$, and 7.9 % for $V_{disp}^{fit}/V_{pp}^{fit}$.

Noise and extraneous lines are particularly troublesome for methods that rely on a few measurements instead of a fit. The details of the errors depend on the method. We illustrate by considering the effect of measuring just one point, the minimum value of the spectrum. Even without noise, the value of the minimum is in error by 13.2 % while the same error is reduced to 3.3 % for the fitted minimum. With noise, measuring one point is out of the question. Residuals, such as those in Fig. 11b, at the least, indicate the presence of an extraneous line that might not be suspected without a fit, so that one can try to account for it or be aware that systematic errors are likely. Clearly one has to be careful, because, in our simple example, a line due to a species at only 3 % of the concentration of the main species leads to significant errors.

The concept of "fitting right through" an extraneous line has an intuitive appeal and comparing the true extraneous line with the residual shows that they are similar, but not same. Such residuals are common in experimental spectra; for example, Fig. 3 and 4 of ref [23] and Fig. 5 of ref [33]. In those cases, the residuals were attributed to ^{13}C because they appeared at the expected resonance fields; however, the shapes were distorted. Fig. 12.

Discussion

The central purpose of this paper was to propose a simple, analytical approximation to an IHB dispersion manifold, Eq. (16). The fidelities of Eq. (16) and the well-known Eq. (2) were tested with separate dispersion and absorption manifolds simulated using the Tempone pattern and admixtures of these were fit to Eq. (20). Because the input values are known, the errors in using these fits are well defined and are detailed above. When contemplating those errors, it is prudent to bear in mind that proceeding without taking into account the IHB leads to errors in ΔH_{pp}^{L} from 8–204 % for $\chi = 0.3$ to 2.5.

By examining the residuals from fits as detailed in Fig. 2 and a comparable figure for the absorption manifolds (not shown), a better criterion for the value of χ_{inc} emerges as the point at which narrow residuals are no longer evident; in the case of Tempone, $\chi_{inc} < 2.0$. Spectra falling into this range are unresolved.

Perhaps Eq. (16) will find use to analyzed pure dispersion lines. If that's the case, then it might be justified to apply it to other patterns or even the Voigt itself to produce a map appropriate to the problem. This would be straightforward following the procedures detailed here.

Equation (20) will certainly find use for admixtures and it may be justified to develop maps based on other patterns. Particularly interesting might be the Universal Nitroxide pattern defined in section 5.2 of ref [6] because it is a good compromise between many nitroxide patterns and is unresolved up to $\chi_{inc} = 6$. Based on our experience, it may not be useful to develop a map based on the Voigt itself, because, even though the Voigt fits many, even most, patterns well, yielding accurate values of the value of ΔH_{pp}^{0}, the values of χ, and therefore, ΔH_{pp}^{L} and ΔH_{pp}^{L}, are not accurate for $\chi > 2$ [6]. One could formulate a map from the Voigt values of χ to the correct values, but, other than the fact that it is justifiable from first principles, there does not seem to be any advantage over the sum- function approximations and, of course, Voigts are cumbersome to compute.

The reader has probably noticed that for admixtures, we rely on the absorption component to separate ΔH_{pp}^{L} and ΔH_{pp}^{G}; i.e., the map to χ is formulated using η_{abs}. For admixtures, the utility of Eq. (16) is to obtain an accurate value of V_{disp}^{fit} and an accurate shape so as not to interfere with the fit parameters of the absorption component of Eq. (20). The fidelity of Eq. (20) shows that this last requisite is fulfilled very well, Fig. 10. There might be use for all the information from both components, for example, for methods that collect both dispersion and absorption components separately [34]. In that event, the map for dispersion manifolds, Table 3, could find use.

We have not investigated the accuracy of Eq. (16) to obtain the relative concentration of a species using the dispersion-only signal because, for admixtures, the absorption component yields the necessary information accurately [6].

Summary of algorithm to treat admixtures

For a cw-EPR spectrum of an admixture, our suggested algorithm to extract accurate values of the important parameters is as follows:

1. Fit the admixture with Eq. (20) to obtain η_{abs}, ΔH^0_{pp}, V^{fit}_{pp}, and $V^{fit}_{disp}/V^{fit}_{pp}$.
2. Find χ from η_{abs} using Table 4 or Eq. (19).
3. Separate ΔH^L_{pp} and ΔH^G_{pp} using χ and ΔH^0_{pp} employing Eqs. (9b) and (1).
4. Compute V_{disp}/V_{pp} from $V^{fit}_{disp}/V^{fit}_{pp}$ using Eq. (21) employing $\theta(\chi)$ from Table 5 or Eq. (22).

If one wishes to correct for IHB to calculate the rotational correlation time, doubly-integrated intensity, concentration of a broadening agent, or assess the purity of deuteration, the procedures of ref [6] are available with knowledge of χ, ΔH^0_{pp}, and V^{fit}_{pp}.

Conclusions

A simple analytical approximation to an IHB dispersion signal has been developed, tested, and shown to be accurate. Combining the new approximation to IHB dispersion with the well-known approximation to IHB absorption has allowed the development of an algorithm to analyze dispersion-absorption admixtures from which accurate parameters appropriate to each individual component may be extracted rapidly. The algorithm is robust in handling admixtures with up to 40 % noise, returning mean values of the parameters that are correct to within the standard deviations in a typical run of 5 spectra. It is also useful to detect an unsuspected underlying extraneous line and reduce the errors provoked by its presence.

Compliance with ethical standards

Conflict of interest The authors declare that they have no competing interests.

References

1. Portis, A. M. (1953). Electronic Structure of F Centers: Saturation of the Electron Spin Resonance. *Physical Review*, *91*, 1071.
2. Wertheim, G. K., Butler, M. A., West, K. W., & Buchanan, D. N. E. (1974). Determination of the Gaussian and Lorentzian Content of Experimental Line Shapes. *Review of Scientific instruments*, *45*, 1369–1371.
3. v.d. Hulst, H. C., & Reesinck, J. J. M. (1947). Lin Breadths and Voigt Profiles. *Astronomical Journal*, *106*, 121–127.
4. Westberg, J., Wang, J., & Axner, O. (2012). Fast and non-approximate methodology for calculation of wavelength-modulated Voigt lineshap functions suitable for real-time curve fitting. *Journal of Quantitative Spectroscopy & Radiative Transfer*, *113*, 2049–2057.
5. Westberg, J., Wang, J., & Axner, O. (2014). Methodology for fast curve fitting to modulated Voigt dispersion lineshape functions. *Journal of Quantitative Spectroscopy & Radiative Transfer*, *133*, 244–250.
6. Bales, B. L. (1989). Inhomogeneously Broadened Spin-Label Spectra. In L. J. Berliner, J. Reuben (Ed.). *Biological Magnetic Resonance* (pp. 77–130). New York: Plenum.
7. Bales, B. L., Peric, M., & Lamy-Freund, M. T. (1998). Gaussian line broadening induced by unresolved proton hyperfine structure and by field modulation into the EPR spectrum of the proxyl spin probe. *Journal of Magnetic Resonance*, *132*, 279–286.
8. Halpern, H. J., Peric, M., Yu, C., & Bales, B. L. (1993). Rapid Quantitation of Parameters from Inhomogeneously Broadened EPR Spectra. *Journal of Magnetic Resonance*, *103*, 13–22.
9. Bales, B. L., & Willett, D. (1984). EPR investigation of the intermediate spin exchange regime. *Journal of Chemical Physics*, *80*, 2997–3004.
10. De Tommasi, E., Castrillo, A., Casa, G., & Gianfrani, L. (2008). An efficient approximation for a wavelength-modulated 2nd harmonic lineshape from a Voigt absorption profile. *Journal of Quantitative Spectroscopy and Radiative Transfer*, *109*, 168–175.
11. Smirnov, A. I., & Belford, R. L. (1995). Rapid Quantitation from Inhomogeneously Broadened EPR Spectra by a Fast Convolution Algorithm. *Journal of Magnetic Resonance A, , 113*, 65–73.
12. Liu, Y., Lin, J., Huang, G., Guo, Y., & Duan, C. (2001). Simple empirical analytical approximation to the Voigt profile. *Journal of Optical Society of America B*, *18*, 666–672.
13. Kielkopf, J. F. (1973). New approximation to the Voigt function with applications to spectral-line analysis. *Journal of Optical Society of America*, *63*, 987–995.
14. Shin, B. (2016). An analytical method for the deconvolution of Voigtian profiles. *Applied Magnetic Resonance*, *47*, 429–452.
15. Klug, C. S., Camenisch, T. G., Hubbell, W. L., & Hyde, J. S. (2005). Multiquantum EPR spectroscopy of spin-labled Arrestin K267c at 35 GHz. *Biophysical Journal*, *88*, 3641–3647.
16. Fajer, P., & Marsh, D. (1983). Analysis of dispersion-mode saturation transfer ESR spectra. Application of model membranes. *Journal of Magnetic Resonance*, *55*, 205–215.
17. Rinard, G. A., Quine, R. W., Ghim, B. T., Eaton, S. S., & Eaton, G. R. (1996). Dispersion and superheterodyne EPR using a bimodal resonator. *Journal of Magnetic Resonance A*, *122*, 58–63.
18. Hyde, J. S., Froncisz, W., & Kusumi, A. (1982). Dispersion electron spin resonance with the loop gap resonator.. *Review of Scientific Instruments*, *53*, 1934–1937.
19. Bales, B. L., & Peric, M. (1997). EPR Line Shifts and Line Shape Changes Due to Spin Exchange of Nitroxide Free Radicals in liquids. *Journal of Physical Chemistry B*, *101*, 8707–8716.
20. Bales, B. L., & Peric, M. (2002). EPR Line Shifts and Line Shape Changes Due to Spin Exchange of Nitroxide Free Radicals in Liquids 2. Extension to High Spin Exchange Frequencies and Inhomogeneously Broadened Spectra. *Journal of Physical Chemistry A*, *106*, 4846–4854.
21. Bales, B. L., Peric, M., & Dragutan, I. (2003). EPR Line Shifts and Line Shape Changes Due to Spin Exchange of Nitroxide Free Radicals in Liquids 3. Extension to Five Hyperfine Lines. Additional Line Shifts Due to Re-encounters. *Journal of Physical Chemistry A*, *107*, 9086–9098.
22. Bales, B. L., Meyer, M., Smith, S., & Peric, M. (2008). EPR Line Shifts and Line Shape Changes Due to Spin Exchange of Nitroxide-Free Radicals in Liquids 4. Test of a Method to Measure Re-encounter Rates in Liquids Employing 15N and 14N Nitroxide Spin Probes. *Journal of Physical Chemistry A*, *112*, 2177–2181.
23. Bales, B. L., Meyer, M., Smith, S., & Peric, M. (2009). EPR Line Shifts and Line Shape Changes Due to Spin Exchange of

Nitroxide-Free Radicals in Liquids 6. Separating Line Broadening due to Spin Exchange and Dipolar Interactions. *Journal of Physical Chemistry A*, *113*, 4930–4940.
24. Bales, B. L., Harris, F. L., Peric, M., & Peric, M. (2009). EPR Line Shifts and Line Shape Changes Due to Spin Exchange of Nitroxide-Free Radicals in Liquids 7. Singly Charged Surfactant Nitroxide. *Journal of Physical Chemistry A*, *113*, 9295–9303.
25. Bales, B. L., Meyer, M., & Peric, M. (2014). EPR Line Shifts and Line Shape Changes Due to Heisenberg Spin Exchange and Dipole–Dipole Interactions of Nitroxide Free Radicals in Liquids: 9. An Alternative Method to Separate the Effects of the Two Interactions Employing 15N and 14N. *Journal of Physical Chemistry A*, *118*, 6154–6162.
26. Salikhov, K. M. (2010). Contributions of Exchange and Dipole-Dipole Interactions to the Shape of EPR Spectra of Free Radicals in Diluted Sollutions. *Applied Magnetic Resonance*, *38*, 237–256.
27. Salikhov, K. M., Mambetov, A. Y., Bakirov, M. M., Khairuzhdinov, I. T., Galeev, R. T., Zaripov, R. B., & Bales, B. L. (2014). Spin Exchange Between Charged Paramagnetic Paritcles in Dilute Solutions. *Applied Magnetic Resonance*, *45*, 911–940.
28. Peric, M., Bales, B. L., & Peric, M. (2012). Electron Paramagnetic Line Shifts and Line Shape Changes Due to Heisenberg Spin Exchange and Dipole-Dipole Interactions of Nitroxide Free Radicals in Liquids 8. Further Experimental and Theoretical Efforts to Separate the Effects of the Two Interactions. *Journal of Physical Chemistry A*, *116*, 2855–2866.
29. Kurban, M. R., Peric, M., & Bales, B. L. (2008). Nitroxide spin exchange due to re-encounter collisions in a series of n-alkanes. *Journal of Chemical Physics*, *129*, 064501–064510.
30. Reif, F. (1965). *Fundamentals of Statistical and Thermal Physics*. New York: McGraw-Hill.
31. Dobryakov, S. N., & Lebedev, Y. S. (1969). Analysis of Spectral Lines whose Profile is Describe by a Composition of Gaussian and Lorentz Profiles. *Soviet Physics-Doklady*, *13*, 873.
32. Ludowise, P., Eaton, S. S., & Eaton, G. R. (1991). A Convenient Monitor of EPR Automatic Frequency Control (AFC) Function. *Journal of Magnetic Resonance*, *93*, 410–412.
33. Smirnov, A. I. (2008). Post-processing of EPR spectra by convolution filtering: Calculation of a harmonics' series and automatic separation of fast-motion components from spin label EPR spectra. *Journal of Magnetic Resonance*, *190*, 154–159.
34. Tseitlin, M., Quine, R. W., Rinard, G. A., Eaton, S. S., & Eaton, G. R. (2010). Combining absorption and dispersion signals to improve singal-to-noise for rapid scan EPR imaging. *Journal of Magnetic Resonance*, *203*, 305–310.